

Numerical Simulation of Transient 3-D Surface Deformation of a Completely Penetrated GTA Weld

An analytical model that explores the dynamic behavior of a weld pool will help in the development of a sensor that detects complete joint penetration in gas tungsten arc welding

BY C. S. WU, P. C. ZHAO, AND Y. M. ZHANG

ABSTRACT. By establishing the correlation between transient behavior of a weld pool surface deformation and workpiece penetration, and quantitatively analyzing the surface deformation at the top and bottom surfaces at the moment the pool penetrates and their dynamic responses to welding process parameters will provide basic data for the development of topside vision-based penetration control in gas tungsten arc welding (GTAW). A transient numerical model was developed to investigate the dynamic behavior of a completely penetrated GTAW joint. A complete and comprehensive scheme was used in which many factors, such as moving arc, 3-D fluid and heat flow fields, transient state, completely penetrated weld, and surface deformation at both the top and bottom surfaces were considered. The transient development of 3-D surface deformation and shape of a weld pool during the period from partial penetration to complete penetration is predicted. The simulated results showed that the ratio curves of the maximum depression to the length and width at the top surface of the weld pool at different times clearly indicated basic information on penetration. Therefore, the relation of the ratios vs. time can be used as an indicator to judge whether the joint is penetrated.

Introduction

Gas tungsten arc welding (GTAW) is the most used arc welding process for critical and accurate joining. For this process, 100% complete joint penetration must be ensured without melt-through or over-penetration (Ref. 1). To this end, auto-

mated sensing and control of the GTAW process must be realized (Ref. 2). In practice, the backside weld bead width is usually employed to determine the extent of penetration. Although the backside bead width can be sensed by a backside sensor, there are limitations of access and coordinating the motion between the torch and sensor, and it is often necessary that the sensor be attached to and moved with the torch to form a weld-face or topside sensor. However, the invisibility of the backside and the strong arc light radiation together cause tremendous difficulties for such sensors. To find a feasible sensor for automated control, various methods have been studied, including pool oscillation (Ref. 3), ultrasound (Ref. 4), and an infrared sensor (Ref. 5). Although significant progress has been made, practical applications are still restricted.

Weld pool behavior contains enough information on penetration. The pool surface is deformed because of the plasma impingement. Previous researchers have found that the resultant depression of the weld pool surface correlates to the penetration depth of the weld pool (Refs. 6–8), but there is a lack of quantitative analysis of such a correlation. Establishing the correlation between dynamic behavior of weld pool surface deformation and the penetration information, while quantitatively analyzing the surface deformation at the top and bottom surfaces when the joint

is penetrated and their dynamic response to welding process parameters will provide much basic data for the realization of a topside vision-based penetration control for the GTAW process. Thus, numerical simulation of the surface deformation and its dynamic behavior to the GTAW process is of great significance for designing the process control algorithm.

Although there have been significant advances in the numerical simulation of the GTAW process (Refs. 9–24), little attention has been paid to the transient dynamics of the 3-D weld pool surface deformation at both the topside and backside of a fully penetrated weld pool and its correlation to the extent of penetration. Previous studies have shown that the pool depression has a direct effect on the penetration (Refs. 6–8). In fact, the weld pool surfaces at both the front and back are depressed when there is complete penetration, and the amplitude of such depression could be a reflection of the extent of penetration (Refs. 25, 26). For dynamic control, quantitative analysis is required to reveal how the process variables (weld pool geometry and surface depression) change with the welding parameters (welding current and velocity). In this paper, a numerical model is developed to describe the transient behavior of a 3-D GTA weld pool with complete penetration and surface deformation, and the quantitative relationship between the pool surface depression at the front side and the extent of penetration.

Formulation

In order to describe the development of weld pool shape, surface deformation, thermal field, and fluid flow field, a GTAW arc is considered to be impinging on the workpiece along the z direction and it moves in the x direction at a constant speed u_0 . A moving (x, y, z) coordinate sys-

KEY WORDS

Weld Pool
Surface Deformation
Penetration
Correlation
Numerical Simulation

C. S. WU and P. C. ZHAO are with Institute of Materials Joining, Shandong University, Jinan, China, wucs@sdu.edu.cn. Y. M. ZHANG is with Center for Manufacturing and Department of Electrical and Computer Engineering, University of Kentucky, Lexington, Ky.

tem is so chosen that its origin is located at the intersection between the arc centerline and the workpiece surface. For such a three-dimensional transient problem, the governing equations include the energy, momentum, and continuity equations. Because of the surface deformations at both topside and backside of the weld pool, some new boundaries appeared at both top and bottom surfaces, and their positions changed with time. Therefore, the calculation domain is no longer a regular rectangular one, which causes some boundary conditions to be difficult to deal with. To represent the irregular boundaries, a coordinate transformation is adopted. The independent variable in transformed space (z^*) is related to the vertical coordinate in physical space (z) according to

$$z^* = \frac{z - F(x, y, t)}{B(x, y, t) - F(x, y, t)} \quad (1)$$

where $F(x, y, t)$ and $B(x, y, t)$ are functions that define the upper and lower surfaces of the weld pool, respectively. The transformation maps the irregularly shaped regions into rectangular computational domains in which the two curvilinear surfaces are stationary during any given time interval, and are defined by $z^* = 0$ and $z^* = 1$. Then, the governing equations describing the fluid flow and heat transfer phenomena in a weld pool are expressed as:

$$\nabla \vec{V} + \frac{\partial \vec{V}}{\partial z^*} \cdot \nabla z^* = 0 \quad (2)$$

$$\rho \frac{\partial \vec{V}}{\partial t} + \rho (\vec{V}_l \cdot \nabla_*) \vec{V} = \vec{F}_b - \left(\nabla p + \frac{\partial p}{\partial z^*} \cdot \nabla z^* \right) + \mu \nabla_s^2 \vec{V} + \vec{C}_v \quad (3)$$

$$\rho c_p \left(\frac{\partial T}{\partial t} + \vec{V}_l \cdot \nabla_* T \right) = \nabla_s (k \nabla_s T) + k C_T \quad (4)$$

where ∇ is the fluid velocity vector with the components (u, v, w) in $x, y,$ and z directions, \vec{V}_l is the fluid velocity vector with the components (u, v, w_l) in $x, y,$ and z directions, \vec{V}_i is the fluid velocity vector with the components (u, v, w_i) in $x, y,$ and z directions, ρ is the density, c_p is the specific heat, p is the pressure, μ is the viscosity, k is the thermal conductivity, and other symbols are defined as follows:

$$\nabla = \frac{\partial}{\partial x} \vec{i} + \frac{\partial}{\partial y} \vec{j} + \frac{\partial}{\partial z} \vec{k} \quad (5)$$

$$\nabla_* = \frac{\partial}{\partial x} \vec{i} + \frac{\partial}{\partial y} \vec{j} + \frac{\partial}{\partial z^*} \vec{k} \quad (6)$$

Table 1 — Other Thermophysical Properties and Parameters Used in the Calculation

Property or Parameter	Symbol	Value
Melting point	T_m	1763 K
Ambient temperature	T_a	293 K
Density	ρ	7200 kg m ⁻³
Latent heat of vaporization	L_b	73.43 × 10 ⁶ J kg ⁻¹
Gravitational acceleration	g	9.8 m s ⁻²
Surface radiation emissivity	ϵ	0.4
Magnetic permeability	μ_m	1.66 × 10 ⁻⁶ H m ⁻¹
Surface tension	γ	1.0 N m ⁻¹
Temperature coefficient of surface tension	$\frac{\partial \gamma}{\partial T}$	-1.12 × 10 ⁻⁴ N m ⁻¹ K ⁻¹
Thermal expansion coefficient	β	10 ⁻⁴
Current density distribution parameter	σ_j	1.5 mm
Heat flux distribution parameter	σ_q	2.25 mm
Arc power efficiency	η	0.65
Plate thickness	H	3 mm

$$\nabla_s = \frac{\partial}{\partial x} \vec{i} + \frac{\partial}{\partial y} \vec{j} + S \frac{\partial}{\partial z^*} \vec{k} \quad (7)$$

$$w_l = \vec{V} \cdot \nabla z^* - \frac{\mu}{\rho} \nabla_s^2 z^* \quad (8)$$

$$w_i = \vec{V} \cdot \nabla z^* - \frac{k}{\rho c_p} \nabla_s^2 z^* \quad (9)$$

$$\vec{C}_v = 2\mu \left[\nabla_{xy} \left(\frac{\partial \vec{V}}{\partial z^*} \right) \right] \cdot \nabla_{xy} z^* \quad (10)$$

$$C_T = 2\mu \left[\nabla_{xy} \left(\frac{\partial T}{\partial z^*} \right) \right] \cdot \nabla_{xy} z^* \quad (11)$$

$$\nabla_{xy} = \frac{\partial}{\partial x} \vec{i} + \frac{\partial}{\partial y} \vec{j} \quad (12)$$

For the body force term,

$$\vec{F}_b = \vec{J} \times \vec{B}_m - \rho \beta g (T - T_\infty) \quad (13)$$

where β is the volume expansion coefficient, g is the acceleration of gravity, T_a is the ambient temperature, and the electromagnetic force $\vec{J} \times \vec{B}_m$ is calculated based on Wu's analytical solutions (Refs. 12 and 15) expressed as follows:

$$\begin{aligned} (\vec{J} \times \vec{B}_m)_x &= -\frac{\mu_m I^2}{4\pi^2 \sigma_j^2 r} \exp\left(-\frac{r^2}{2\sigma_j^2}\right) \\ &\quad \left[1 - \exp\left(-\frac{r^2}{2\sigma_j^2}\right) \right] \left(1 - \frac{z}{H} \right)^2 \frac{x}{r} \end{aligned} \quad (14)$$

$$\begin{aligned} (\vec{J} \times \vec{B}_m)_y &= -\frac{\mu_m I^2}{4\pi^2 \sigma_j^2 r} \exp\left(-\frac{r^2}{2\sigma_j^2}\right) \\ &\quad \left[1 - \exp\left(-\frac{r^2}{2\sigma_j^2}\right) \right] \left(1 - \frac{z}{H} \right)^2 \frac{y}{r} \end{aligned} \quad (15)$$

$$\begin{aligned} (\vec{J} \times \vec{B}_m)_z &= \frac{\mu_m I^2}{4\pi^2 H r^2} \\ &\quad \left[1 - \exp\left(-\frac{r^2}{2\sigma_j^2}\right) \right]^2 \left(1 - \frac{z}{H} \right) \end{aligned} \quad (16)$$

where μ_m is the magnetic permeability, I is the welding current, σ_j is the effective radius of the current distribution in Gaussian form, H is the thickness of the workpiece, and $r = \sqrt{x^2 + y^2}$.

When the workpiece is not completely penetrated, the weld pool has only one free surface $F(x, y, t)$, which is deformed under the combined action of arc pressure, hydrostatic force, and surface tension. If the workpiece is completely penetrated, the weld pool has two free surfaces, i.e., the upper surface $F(x, y, t)$ and the lower surface $B(x, y, t)$.

Under the condition of partial penetration, the shape of weld pool surface $F(x, y, t)$ can be described by the following equation:

$$p_a - \rho g F + C_1 = \gamma \nabla \left(\frac{\nabla F_s}{|\nabla F_s|} \right) \quad (17)$$

where p_a is the plasma arc pressure, C_1 the Langrangian constant, γ the surface tension, and $F_s = z - F(x, y, t) = 0$.

The arc pressure p_a can be described by (Ref. 27)

$$P_{arc} = \frac{\mu_m I J}{4\pi} \quad (18)$$

where J is the current density at the workpiece surface, which can be assumed to be in Gaussian distribution (Ref. 28)

$$J(r) = \frac{I}{2\pi \sigma_j^2} \exp\left(-\frac{r^2}{2\sigma_j^2}\right) \quad (19)$$

Table 2 — Comparison of the Maximum Depression at Top Surface

	Predicted		Measured	
	Weld width (mm)	Depression (mm)	Weld width (mm)	Depression (mm)
Top side	5.4	0.14	6.5	0.12
Bottom side	1.9	0.27	1.7	0.30

(SS304 workpiece, thickness 3 mm, 110 A, 12 V, 125 mm/min)

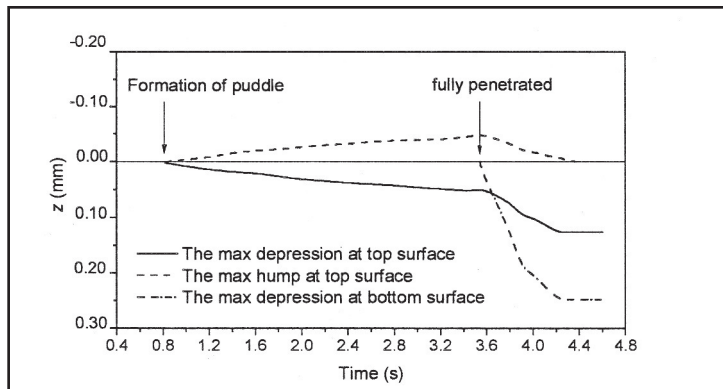


Fig. 1 — The surface deformation vs. time (workpiece, SS304; thickness, 3 mm; 100 A; 14 V; 125 mm/min).

Equation 17 should satisfy with the constraint condition

$$\iint_{S_T} F \, dx dy = 0 \quad (20)$$

where S_T is the area of fusion zone at the workpiece's upper surface ($z = 0$), i.e., the domain of $F(x,y,t)$ at the plane $z = 0$. The Langrangian constant C_1 can be determined by using Equation 20.

If the workpiece is completely penetrated, the upper surface $F(x,y,t)$ and the lower surface $B(x,y,t)$ of the weld pool can be expressed as

$$p_a - \rho g F + C_2 = \gamma \nabla \left(\frac{\nabla F_s}{|\nabla F_s|} \right) \quad (21)$$

$$\rho g (B - F) + C_2 = \gamma \nabla \left(\frac{\nabla B_s}{|\nabla B_s|} \right) \quad (22)$$

where $B_s = z - B(x,y,t) = 0$, and C_2 is the Langrangian constant, to make Equations 21 and 22 satisfactory with the constraint condition

$$\iint_{S_T} F \, dx dy - \iint_{S_B} B \, dx dy = 0 \quad (23)$$

where S_B is the area of the fusion zone at the workpiece's lower surface ($z = H$), i.e., the domain of $B(x,y,t)$ at the plane $z = H$.

In transient state, the weld pool geometry changes with time t , so the domains S_T and S_B also vary with time. In this way, the variations of $F(x,y,t)$ and $B(x,y,t)$ with time t are described.

The boundary conditions for solving the governing Equations 2–4 are as follows:

For the free surface of weld pool,

$$\mu \frac{\partial u}{\partial z^*} \frac{\partial z^*}{\partial z} = - \frac{\partial \gamma}{\partial T} \frac{\partial T}{\partial x} \quad (24)$$

$$\mu \frac{\partial v}{\partial z^*} \frac{\partial z^*}{\partial z} = - \frac{\partial \gamma}{\partial T} \frac{\partial T}{\partial y} \quad (25)$$

$$w = 0 \quad (26)$$

$$-k \frac{\partial T}{\partial z^*} \frac{\partial z^*}{\partial z} = q_{arc} - q_{cr} - q_{evp} \quad (27)$$

when,

$$\begin{aligned} (x - u_0 t) \geq 0, \quad q_{arc}(x, y) &= \frac{6\eta EI}{\pi a(b_1 + b_2)} \\ \exp\left[-\frac{3(x - u_0 t)^2}{b_1^2}\right] \exp\left(-\frac{3y^2}{a^2}\right) & \quad (28) \end{aligned}$$

when,

$$\begin{aligned} (x - u_0 t) < 0, \quad q_{arc}(x, y) &= \frac{6\eta EI}{\pi a(b_1 + b_2)} \\ \exp\left[-\frac{3(x - u_0 t)^2}{b_2^2}\right] \exp\left(-\frac{3y^2}{a^2}\right) & \quad (29) \end{aligned}$$

$$q_{cr} = h_{cr}(T - T_\infty) \quad (30)$$

$$q_{evp} = m_{er} L_b \quad (31)$$

where $a(b_1 + b_2) = 12\sigma_q^2$, $a = 1.87\sigma_q$, $b_1 = 2.51\sigma_q$, $b_2 = 3.91\sigma_q$, η the arc power efficiency, E the arc voltage, and σ_q the distribution parameter of arc heat flux. In this research, h_{cr} is the combined heat transfer coefficient for the convection and radiation boundary, T_∞ is the ambient temperature, L_b is the latent heat of evaporation, and m_{er} is the evaporation mass rate. For a metal such as steel, h_{cr} and m_{ev} can be written as (Refs. 29, 30)

$$h_{cr} = 24.1 \times 10^{-4} \varepsilon T^{1.61} \quad (32)$$

$$\log(m_{ev}) = A - B/T - 0.5 \log T \quad (33)$$

where ε is the emissivity of the workpiece surface, and A and B are constants ($A = 8.641$, $B = 18836$).

For the symmetric plane ($y = 0$),

$$\frac{\partial \vec{V}}{\partial y} = 0, \quad \frac{\partial T}{\partial y} = 0 \quad (34)$$

In the solid,

$$\vec{V} = 0 \quad (35)$$

The boundary conditions for Equations 19, 21, and 22 are written as:

For the domain outside the melting zone,

$$F = 0, \quad B = 0 \quad (36)$$

For the points at the melting zone boundary on the oxz -plane,

$$\frac{\partial F}{\partial x} = 0, \quad \frac{\partial B}{\partial x} = 0 \quad (37)$$

For the initial conditions:

$$\begin{aligned} t = 0, \quad T(x, y, z, 0) &= T_0, \\ F(x, y, 0) = 0, \quad B(x, y, 0) &= 0 \quad (38) \end{aligned}$$

Methods of Solution

The governing equations and boundary conditions are solved by means of the finite difference technique. The scheme of differences has a high degree of nonlinearity, as the characteristic values for the material are taken as temperature-dependent. Coupling occurs between and within the relevant aspects of the problem. Thus, a special iterative procedure is necessitated.

The program first calculates the temperature field in the solid workpiece. Once the melt zone emerges, the whole domain is divided into two regions, i.e., the fluid flow zone in the weld pool and the solid zone outside the pool. The calculations of fluid flow and heat transfer inside the pool and the conductive heat transfer outside the pool are conducted simultaneously. Then, the shape of the weld pool surface is calculated according to the pressure and energy equilibrium conditions. The liquid-solid boundary is determined by the enthalpy at the melting point. Based

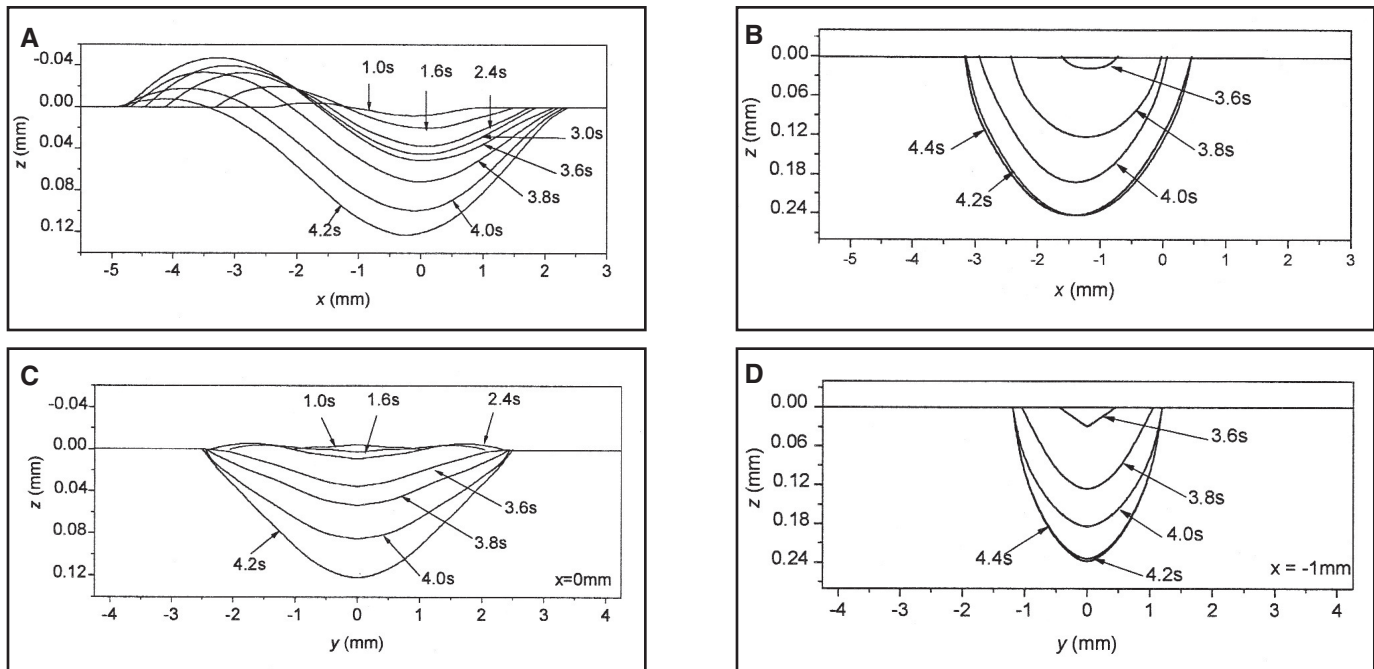


Fig. 2 — The transient development of weld pool surface deformation (workpiece, SS304; thickness, 3 mm; 100 A; 14 V; 125 mm/min). A — Deformation at top surface (side view, enlarged in z direction); B — deformation at bottom surface (side view, enlarged in z direction); C — deformation at top surface (front view, enlarged in z direction); D — deformation at bottom surface (front view, enlarged in z direction).

on the deformed pool surface, the fluid flow and temperature fields are recalculated. Then, the configuration of the weld pool surface and geometry is adjusted, and a repeated calculation procedure commences. Once the workpiece is completely penetrated, the appropriate equilibrium conditions of pressure are applied to determine the shape of the weld pool and its surface deformation at both topside and bottom side. The fluid flow and heat transfer within the pool are recalculated, and the pool geometry is modified. Iterations are performed until the selected convergence criterion is satisfied. The overall algorithm consists of individual procedures which are performed iteratively. The iterative calculations for the transient problems are carried out. At each time step, all physical subprocesses are solved numerically until the convergence criterion is met, and then time is incremented and the calculation procedure is repeated.

The additional source term method is utilized to transform both energy and momentum boundary conditions into discrete forms, and the discrete governing equations in body-fitted coordinates are established. Nonuniform grids are used with finer spacing inside the weld pool and coarser away from it to improve the simulation accuracy and speed up the convergence. Various subprocess problems are calculated separately and improved by turns during the whole iterative procedure. In this way, the strongly coupling problems are solved effectively and successfully.

Results

Numerical simulations are performed for GTAW on stainless steel 304. A half workpiece with a welding domain of $200 \times 50 \times 3$ mm are divided into the mesh of $352 \times 60 \times 10$ grid points. For the 304 material, the specific heat c_p , dynamic viscosity μ , and thermal conductivity k are temperature dependent, which can be expressed as follows (Ref. 31):

$$k = \begin{cases} 10.717 + 0.014955T & T \leq 780K \\ 12.076 + 0.013213T \text{ (W m}^{-1}\text{K}^{-1}\text{)} & 780K \leq T \leq 1672K \\ 217.12 - 0.1094T & 1672K \leq T \leq 1727K \\ 8.278 + 0.0115T & 1727 \leq T \end{cases} \quad (39)$$

$$\mu = \begin{cases} 37.203 - 0.0176T & 1713K \leq T \leq 1743K \\ 20.354 - 0.008T \text{ (} 10^{-3} \text{ kg m}^{-1}\text{s}^{-1}\text{)} & 1743K \leq T \leq 1763K \\ 34.849 - 0.0162T & 1763K \leq T \leq 1853K \\ 13.129 - 0.0045T & 1853K \leq T \leq 1873K \end{cases} \quad (40)$$

$$c_p = \begin{cases} 438.95 + 0.198T & T \leq 773K \\ 137.93 + 0.59T \text{ (J kg}^{-1}\text{)} & 773K \leq T \leq 873K \\ 871.25 - 0.25T & 873K \leq T \leq 973K \\ 555.2 + 0.0775T & 973K \leq T \end{cases} \quad (41)$$

Other thermophysical properties and parameters used in the calculation are summarized in Table 1.

The development of the weld pool includes the following stages: weld pool forming after the arc ignition, the pool expanding, and the pool reaching quasi-

steady state. The welding conditions were as follows:

- 1) Test piece was 304 stainless steel with 250 mm length, 60 mm width, and 3 mm thickness.
- 2) The welding current was 100 A.
- 3) The arc voltage was 14 V.
- 4) The welding speed was 125 mm/min.

The figures and tables denote conditions as workpiece, SS304; thickness, 3 mm; 100 A; 14 V; and 125 mm/s. For the welding conditions used, the weld pool emerges at $t = 0.82$ s, then expands continuously, gets fully penetrated at $t = 3.54$ s, and reaches the quasi-steady state at $t = 4.24$ s. Figure 1 shows the transient development of the pool surface deformation, i.e., the maximum values of the depression at both sides and the hump at the topside vs. time. After the weld pool is formed at $t = 0.82$ s, the pool surface deformation is produced. As the pool volume expands with increasing time, the extent of the pool surface deformation gets bigger, and both maximum depression and hump at topside increase with time. The test plate is completely penetrated $t = 3.54$ s. In the mean time, the bottom surface of the weld pool starts to deform, so the whole weld pool is depressed. Then, the hump at topside decreases, while the depressions at both sides rise at a higher rate. When the thermal process reaches the quasi-steady state at $t = 4.24$ s, the weld pool geometry keeps constant, the hump at the topside becomes zero, and the depressions of the weld pool at both sides attain their maxi-

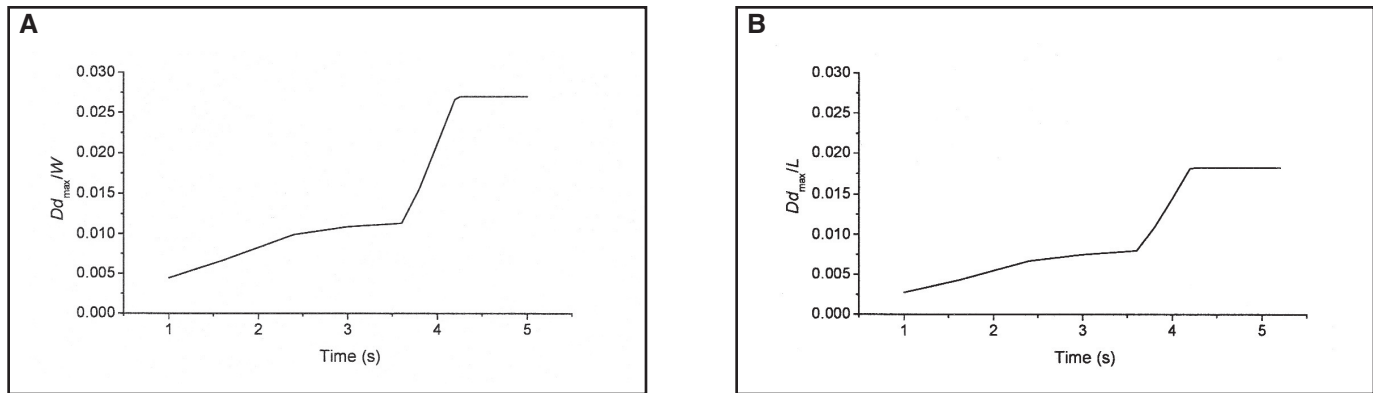


Fig. 3 — The ratios of Dd_{max}/W and Dd_{max}/L vs. time (workpiece, SS304; thickness, 3 mm; 100 A; 14 V; 125 mm/min). A — The ratio of the maximum depression to the pool width; B — the ratio of the maximum depression to the pool length.

imum and do not vary anymore with time. It can be seen that the increasing rate of the pool surface depressions is quite different before and after the pool is completely penetrated.

Figure 2 illustrates the transient development of weld pool surface deformation at both the top and bottom sides of the weld pool. In this figure, A and B are the longitudinal sections (side view), while C and D are the transverse cross sections (front view). Compared to the top surface of the weld pool, the bottom surface gets depressed more seriously and quickly. The maximum depression at the bottom surface increases from 0 mm at $t = 3.54$ s (the moment when the pool is just completely penetrated) to 0.26 mm at $t = 4.24$ s (the instant when the quasi-steady state is reached). The increasing rate is 0.371 mm/s. As shown in Fig. 2D, there is a minor oscillation of the pool surface deformation at the bottom side after the weld pool geometry reaches quasi-steady state. But the amplitude of such oscillation is so low that the bottom surface contours at $t = 4.2$ s and $t = 4.4$ s are nearly identical with each other. For the top surface depression, the increasing rates of maximum depression are 0.031 mm/s before complete penetration (from 0 mm at $t = 0.82$ s to 0.098 mm at $t = 4.0$ s) and 0.117 mm/s after complete penetration (from 0.098 mm at $t = 4.0$ s to 0.126 mm at $t = 4.24$ s), respectively.

Since the variation rate of the top surface depression of the weld pool has a marked increase after the pool is completely penetrated, it can be taken as an indicator to judge whether the plate is penetrated or not. On the other hand, the pool length and width at the topside are also changed after complete penetration is achieved. To quantitatively describe the correlation of the topside surface depression with the extent of penetration, two characteristic variables are used to reflect the variation of the whole weld pool geometry, i.e., the ratio of the maximum de-

pression Dd_{max} to the pool width W (Dd_{max}/W), and the ratio of Dd_{max} to the pool length L (Dd_{max}/L). Figure 3 shows the ratios of Dd_{max}/W and Dd_{max}/L vs. time. The three-segment curves of such ratios reflect the information on the penetration. During the expanding of the non-penetrated weld pool, the values of Dd_{max}/W and Dd_{max}/L rise slowly with time. At the moment the weld pool is fully penetrated ($t = 3.54$ s), the rising rates of Dd_{max}/W and Dd_{max}/L are suddenly increased, i.e., the slopes of two curves increase in a marked way. The first kink point on the curves corresponds to the moment when the weld pool gets fully penetrated. When the quasi-steady state is obtained at $t = 4.24$ s, the weld pool geometry is in a relatively stable condition, Dd_{max}/W and Dd_{max}/L are nearly constant, so the curves are just straight lines after 4.24 s. The second kink point on the curves corresponds to the moment when the weld pool reaches the quasi-steady state. Because the depression of the weld pool surface at the topside has the characteristics mentioned above, it can be employed as an indicator of weld penetration extent. In practice, the topside sensor can be developed to measure the weld pool surface depression for weld penetration control.

Experimental measurements are made to verify the model. After welding, a macrograph of a weld cross section is made to measure the weld dimension. Table 2 is the comparison between the predicted and experimental weld depressions on a weld cross section. They are in agreement with each other.

Conclusions

1) A 3-D transient numerical model is developed for investigating the dynamic behavior of the weld pool geometry, surface deformation, heat transfer, and fluid flow in a full-joint penetrated GTA weld pool. Based on the model, the weld pool

emerges at $t = 0.82$ s, then it expands continuously, gets fully penetrated at $t = 3.54$ s, and reaches the quasi-steady state at $t = 4.24$ s, for the welding conditions used (workpiece, SS304; thickness, 3 mm; 100 A; 14 V; 125 mm/s).

2) For the top surface depression, the increasing rates of maximum depression are 0.031 mm/s before complete penetration (from 0 mm at $t = 0.82$ s to 0.098 mm at $t = 4.0$ s) and 0.117 mm/s after complete penetration (from 0.098 mm at $t = 4.0$ s to 0.126 mm at $t = 4.24$ s), respectively. Compared to the top surface of the weld pool, the bottom surface gets depressed more seriously and quickly, with the maximum depression of 0.26 mm and the increasing rate of 0.371 mm/s.

3) The variation rate of the ratios of the maximum pool surface depression at the topside to the pool width, and to the pool length, can be described if the plate is completely penetrated. The simulation results lay a foundation for topside sensor-based process control of the GTAW process.

Acknowledgments

The authors are grateful for the financial support for this project from United States National Science Foundation under Grant No. DMI-0114982, and The National Natural Science Foundation of China under Grant No. 50475131. They would like to thank T. T. Feng, M. X. Zhang, and J. K. Hu for their help in experiments, and H. G. Wang for his help in graph drawing.

References

1. Swaim, W. 1998. Gas tungsten arc welding made easy. *Welding Journal* 77(9): 51–52.
2. Zhang, Y. M., Kovacevic, R., and Lin, L. 1996. Adaptive control of full penetration GTA welding. *IEEE Trans. on Control Systems Technology* 4(4): 394–403.

3. Xiao, Y. X., and Ouden, G. den 1993. Weld pool oscillation during GTA welding of mild steel. *Welding Journal* 72(8): 428-s to 434-s.
4. Carlson, N. M., and Johnson, J. A. 1988. Ultrasonic sensing of weld pool penetration. *Welding Journal* 67(11): 239-s to 246-s.
5. Wikle, H. C., Kottilingam, S., Zee, R. H., and Chen, B. A. 2001. Infrared sensing techniques for penetration depth control of the submerged arc welding process. *Journal of Materials Processing Technology*, 113: 228–233.
6. Friedman, E. 1978. Analysis of weld puddle distortion and its effect on penetration. *Welding Journal* 57(6): 161-s to 166-s.
7. Lin, M. L., and Eagar, T. W. 1985. Influence of arc pressure on weld pool geometry. *Welding Journal* 64(6): 163-s to 169-s.
8. Rokhlin, S. I., and Guu, A. C. 1993. A study of arc force, pool depression, and weld penetration during gas tungsten arc welding. *Welding Journal* 72(8): 381-s to 390-s.
9. Oreper, G. M., and Szekely, J. 1984. Heat and fluid-flow phenomena in weld pools. *Journal of Fluid Mechanics*, 147(10): 53–79.
10. Oreper, G. M., Szekely, J., and Eagar, T. W. 1986. The role of transient convection in the melting and solidification in arc weldpools. *Metall. Trans. B*, 17: 735–744.
11. Kou, S., and Wang, Y. H. 1986. Computer simulation of convection in moving arc weld pools. *Metall. Trans. A*, 17 (12): 2271–2277.
12. Tsao, K. C., and Wu, C. S. 1988. Fluid flow and heat transfer in GMA weld pools. *Welding Journal* 67(3): 70-s to 75-s.
13. Zacharia, T., David, S. A., Vitek, J. M., and Debroy, T. 1989. Weld pool development during GTA and laser beam welding of type 304 stainless steel, part I — theoretical analysis. *Welding Journal* 68: 499-s to 509-s.
14. Zacharia, T., Eraslan, A. H., Aidun, D. K., and David, S. A. 1989. Three-dimensional transient model for arc welding process. *Metall. Trans. B*, 20(10): 645–659.
15. Wu, C. S., and Tsao, K. C. 1990. Modeling the three-dimensional fluid flow and heat transfer in a moving weld pool. *Engineering Computations* 7(3): 241–248.
16. Zacharia, T., David, S. A., Vitek, J. M., and Debroy, T. 1990. Modeling of interfacial phenomena in welding. *Metall. Trans. B*, 21(6): 600–603.
17. Choo, R. T. C., Szekely, J., and Westhoff, R. C. 1991. Modeling of high-current arcs with emphasis on free surface phenomena in the weld pool. *Welding Journal* 69(9): 346-s to 361-s.
18. Choo, R. T. C., Szekely, J., and David, S. A. 1992. On the calculation of the free surface temperature of gas-tungsten-arc weld pools from first principles: part II modeling the weld pool and comparison with experiments. *Metall. Trans. B*, 23(6): 371–384.
19. Wu, C. S., and Dorn, L. 1994. Computer simulation of fluid dynamics and heat transfer in full-penetrated TIG weld pools with surface depression. *Computational Materials Science*, 2: 341–349.
20. Domey, J., Aidun, D. K., Ahmadi, G., Regel, L., and Wilcox, W. R. 1995. Numerical simulation of the effect of gravity on weld pool shape. *Welding Journal* 74(8): 263-s to 268-s.
21. Wu, C. S., and Zheng, W. 1997. Analysis of fluid flow and heat transfer in a moving pulsed TIG weld pool. *International Journal for the Joining of Materials*, 9: 166–170.
22. Wu, C. S., Sun, J. S. 1998. Determining the distribution of the heat content of filler metal droplet transferred into GMA weld pools. *Proc Instn Mech Engrs, Part B: Journal of Engineering Manufacture*, Vol. 212B, 525–531.
23. Ko, S. H., Choi, S. K., and Yoo, C. D. 2001. Effects of surface depression on pool convection and geometry in stationary GTAW. *Welding Journal* 80: 39-s to 45-s.
24. Wu, C. S., and Yan, F. 2004. Numerical simulation of transient development and diminution of weld pool in gas tungsten arc welding. *Modeling and Simulation in Materials Science and Engineering*, 12: 13–20.
25. Kovacevic, R., and Zhang, Y. M. 1997. Real-time image processing for monitoring of free weld pool surface. *ASME Journal of Manufacturing Science and Engineering*, 119: 161–169.
26. Saeed, G., and Zhang, Y. M. 2003. Mathematical formulation and simulation of specular reflection based measurement system for gas tungsten arc weld pool surface. *Measurement Science and Technology*, 14: 1671–1682.
27. Lin, M. L., and Eagar, T. W. 1986. Pressure produced by gas tungsten arcs. *Metall. Trans. B*, 17(9): 601–607.
28. Tsai, N. S., and Eagar, T. W. 1985. Distribution of the heat and current fluxes in gas tungsten arcs. *Metall. Trans. B*, 16(4): 841–846.
29. Goldak, J., Bibby, M., Moore, J., and Patel, B. 1986. Computer modeling of heat flow in welds. *Metall. Trans.*, 17B: 587–600.
30. Choi, M., and Greif, R. 1987. A study of heat transfer during welding with applications to pure metals or alloys and low or high boiling temperature materials. *Numerical Heat Transfer*, 11: 477–489.
31. Wu, C. S. Computer simulation of three-dimensional convection in traveling MIG weld pools. 1992. *Engineering Computations*, 9(5): 529–537.

CAN WE TALK?

The *Welding Journal* staff encourages an exchange of ideas with you, our readers. If you'd like to ask a question, share an idea or voice an opinion, you can call, write, e-mail or fax. Staff e-mail addresses are listed below, along with a guide to help you interact with the right person.

Publisher/Editor

Andrew Cullison
cullison@aws.org, Extension 249
 Article Submissions

Senior Editor

Mary Ruth Johnson
mjohnsen@aws.org, Extension 238
 Feature Articles

Associate Editor

Howard Woodward
woodward@aws.org, Extension 244
 Society News
 Personnel

Assistant Editor

Kristin Campbell
kcampbell@aws.org, Extension 257
 New Products
 New Literature

Production Editor

Zaida Chavez
zaida@aws.org, Extension 265
 Design and Production

Advertising Sales Director

Rob Saltzstein
salty@aws.org, Extension 243
 Advertising Sales

Advertising Production Coordinator

Frank Wilson
fwilson@aws.org, Extension 465
 Advertising Production

Advertising Sales & Promotion Coordinator

Lea Garrigan
garrigan@aws.org, Extension 220
 Production and Promotion

Peer Review Coordinator

Doreen Kubish
doreen@aws.org, Extension 275
 Peer Review of Research Papers

Welding Journal Dept.
 550 N.W. LeJeune Rd.
 Miami, FL 33126
 (800) 443-9353
 FAX (305) 443-7404